



This is a repository copy of *ALMA reveals a compact and massive molecular outflow driven by the young AGN in a nearby ULIRG.*

White Rose Research Online URL for this paper:

<https://eprints.whiterose.ac.uk/222389/>

Version: Published Version

Article:

Holden, L.R. orcid.org/0000-0002-1721-1918, Tadhunter, C., Audibert, A. et al. (5 more authors) (2024) ALMA reveals a compact and massive molecular outflow driven by the young AGN in a nearby ULIRG. *Monthly Notices of the Royal Astronomical Society*, 530 (1). pp. 446-456. ISSN 0035-8711

<https://doi.org/10.1093/mnras/stae810>

Reuse

This article is distributed under the terms of the Creative Commons Attribution (CC BY) licence. This licence allows you to distribute, remix, tweak, and build upon the work, even commercially, as long as you credit the authors for the original work. More information and the full terms of the licence here:

<https://creativecommons.org/licenses/>

Takedown

If you consider content in White Rose Research Online to be in breach of UK law, please notify us by emailing eprints@whiterose.ac.uk including the URL of the record and the reason for the withdrawal request.



eprints@whiterose.ac.uk
<https://eprints.whiterose.ac.uk/>

ALMA reveals a compact and massive molecular outflow driven by the young AGN in a nearby ULIRG

Luke R. Holden ¹★, Clive Tadhunter,¹ Anelise Audibert,^{2,3} Tom Oosterloo,^{4,5} Cristina Ramos Almeida ^{2,3}, Raffaella Morganti ^{4,5}, Miguel Pereira-Santaella⁶ and Isabella Lamperti ⁷

¹Department of Physics & Astronomy, University of Sheffield, S6 3TG Sheffield, UK

²Instituto de Astrofísica de Canarias, Calle Vía Láctea, s/n, E-38205 La Laguna, Tenerife, Spain

³Departamento de Astrofísica, Universidad de La Laguna, E-38206 La Laguna, Tenerife, Spain

⁴ASTRON, the Netherlands Institute for Radio Astronomy, Oude Hoogeveensedijk 4, NL-7991 PD Dwingeloo, The Netherlands

⁵Kapteyn Astronomical Institute, University of Groningen, Postbus 800, NL-9700 AV Groningen, The Netherlands

⁶Instituto de Física Fundamental, CSIC, Calle Serrano 123, 28006 Madrid, Spain

⁷Centro de Astrobiología (CAB), CSIC-INTA, Ctra. de Ajalvir Km. 4, E-28850 Torrejón de Ardoz, Madrid, Spain

Accepted 2024 March 13. Received 2024 February 20; in original form 2023 December 8

ABSTRACT

The ultraluminous infrared galaxy F13451+1232 is an excellent example of a galaxy merger in the early stages of active galactic nucleus (AGN) activity, a phase in which AGN-driven outflows are expected to be particularly important. However, previous observations have determined that the mass outflow rates of the warm ionized and neutral gas phases in F13451+1232 are relatively modest, and there has been no robust detection of molecular outflows. Using high-spatial resolution Atacama Large Millimeter/submillimeter Array CO(1–0) observations, we detect a kiloparsec-scale circumnuclear disc, as well as extended ($r \sim 440$ pc), intermediate-velocity ($300 < |v| < 400$ km s^{−1}) cold molecular gas emission that cannot be explained by rotational disc motions. If interpreted as AGN-driven outflows, the mass outflow rates associated with this intermediate-velocity gas are relatively modest ($\dot{M}_{\text{out}} = 22\text{--}27 M_{\odot} \text{ yr}^{-1}$); however, we also detect a compact ($r_{\text{out}} < 120$ pc), high-velocity ($400 < v < 680$ km s^{−1}) cold molecular outflow near the primary nucleus of F13451+1232, which carries an order of magnitude more mass ($\dot{M}_{\text{out}} \sim 230 M_{\odot} \text{ yr}^{-1}$) than (and several times the kinetic power of) the previously detected warmer phases. Moreover, the similar spatial scales of this compact outflow and the radio structure indicate that it is likely accelerated by the small-scale ($r \sim 130$ pc) AGN jet in the primary nucleus of F13451+1232. Considering the compactness of the nuclear outflow and intermediate-velocity non-rotating gas that we detect, we argue that high-spatial resolution observations are necessary to properly quantify the properties of AGN-driven outflows and their impacts on host galaxies.

Key words: galaxies: active – galaxies: evolution – galaxies: individual: F13451+1232 – ISM: jets and outflows – quasars: general – galaxies: interactions.

1 INTRODUCTION

Although often required by models of galaxy evolution to explain the observed properties of the galaxy population (e.g. Magorrian et al. 1998; Silk & Rees 1998; Di Matteo, Springel & Hernquist 2005; Davé et al. 2019), considerable uncertainties remain regarding the impact of gas outflows driven by active galactic nuclei (AGN). Principally, this is because outflow masses and kinetic powers are often not precisely determined (see Harrison et al. 2018), and their dominant driving mechanisms (radiation pressure e.g. Hopkins & Elvis 2010; Meena et al. 2023, or jet-interstellar medium (ISM) interactions e.g. Mukherjee et al. 2016; Audibert et al. 2023) in different object types are unclear.

An excellent object to investigate the impact and launching mechanism(s) of AGN-driven outflows is the ultraluminous infrared galaxy

(ULIRG; $L_{\text{IR}} > 10^{12} L_{\odot}$; Sanders & Mirabel 1996) F13451+1232 – also known as 4C12.50 – which is a merger (Gilmore & Shaw 1986; Heckman et al. 1986) in a late pre-coalescence phase (nuclear separation ~ 4.5 kpc; Tadhunter et al. 2018). ULIRGs such as F13451+1232 are among the most rapidly evolving galaxies in the local universe due to merger-induced gas inflows feeding the central AGN and triggering star formation – the exact situation modelled in some hydrodynamic simulations of galaxy evolution that include AGN-driven outflows as a feedback mechanism (e.g. Di Matteo et al. 2005; Hopkins et al. 2008).

As a luminous radio source ($L_{1.4\text{GHz}} = 1.9 \times 10^{26}$ W Hz^{−1}), F13451+1232 contains radio emission on two distinct scales: small-scale emission within a radius of ~ 130 pc of the primary nucleus along position angle PA = 151° (Stanghellini et al. 1997; Lister et al. 2003; Morganti et al. 2013), and larger scale, diffuse emission extending to a radial distance of ~ 77 kpc from the primary nucleus along PA $\sim 180^{\circ}$ (Stanghellini et al. 2005). It has been proposed that

* E-mail: lholden2@sheffield.ac.uk

this radio structure could be the result of two epochs of jet activity (Stanghellini et al. 2005), with the smaller scale radio structure comprising a young, recently restarted jet, and the larger scale emission originating from a previous jet cycle.

Because of the properties of its small-scale radio emission, F13451+1232 is also classified as a gigahertz-peaked-spectrum (GPS) source (see O’Dea & Saikia 2021 for a review); such sources are associated with powerful jet-ISM interactions that may accelerate gas outflows in multiple phases (Holt et al. 2006; Mukherjee et al. 2016; Santoro et al. 2018, 2020; Kukreti et al. 2023). In addition, given the object’s high-optical emission-line luminosity ($L_{[\text{O III}]}$ = 1.45×10^{43} erg s $^{-1}$; Rose et al. 2018) – leading to its additional classification as a type-2 quasar (QSO2)¹ – it might also be expected to accelerate outflows via radiation-pressure-driven winds.

Despite the fact that outflows in F13451+1232 have been confirmed in the coronal (Villar Martín et al. 2023), warm ionized (Holt, Tadhunter & Morganti 2003; Holt et al. 2011; Rose et al. 2018; Villar Martín et al. 2023), and neutral atomic (HI + Na I D; Morganti, Tadhunter & Oosterloo 2005; Rupke, Veilleux & Sanders 2005; Morganti et al. 2013) gas phases, there has so far not been a robust detection of molecular outflows in this object (Fotopoulou et al. 2019; Lamperti et al. 2022; see discussion in Villar Martín et al. 2023). In nearby AGN where molecular outflows have been detected, it is often found that they contain more mass and kinetic power than the warmer phases (e.g. Fiore et al. 2017; Ramos Almeida et al. 2019; Holden & Tadhunter 2023; Holden et al. 2023; Speranza et al. 2024). In this context, it is important to note that the warm ionized and neutral atomic outflows in F13451+1232 have relatively modest mass outflow rates ($\sim 6\text{--}12 M_{\odot} \text{ yr}^{-1}$; Morganti et al. 2013; Rose et al. 2018); therefore, if molecular outflows are present, they could potentially carry enough mass to change the interpretation of AGN feedback in this important object.

A cold molecular outflow in a similar source, PKS 1549–79, was found to be compact ($r < 120$ pc; Oosterloo et al. 2019), as were the previously detected neutral HI ($r_{\text{HI}} < 100$ pc; Morganti et al. 2013) and warm ionized ($r_{[\text{O III}]}$ ~ 69 pc; Tadhunter et al. 2018) outflows in F13451+1232. Therefore, here we present high-spatial resolution (0.113×0.091 arcsec or 247×119 pc beam size), high-sensitivity Atacama Large Millimeter/submillimeter Array (ALMA) observations of the inner few kiloparsecs of the primary nucleus of F13451+1232 to search for (and characterize) cold molecular outflows in CO(1–0) emission.

In Section 2, we describe the ALMA CO(1–0) observations and our data reduction process; in Section 3 we detail our analysis of the cold molecular gas in the central kiloparsecs of F13451+1232; in Section 4 we discuss our findings and their wider implications, and in Section 5 we give our conclusions.

Throughout this work, we assume a cosmology with $H_0 = 70 \text{ km s}^{-1} \text{ Mpc}^{-1}$, $\Omega_m = 0.3$, and $\Omega_{\lambda} = 0.7$. This corresponds² to an arcsec-to-kpc spatial conversion factor of 2.189 kpc/arcsec and a luminosity distance of $D_L = 570$ Mpc at the redshift of F13451+1232 ($z = 0.121680$; Lamperti et al. 2022).

¹F13451+1232 is included in the QUADROS sample of ULIRGs (Rose et al. 2018), and the QSOFEED sample of type-2 quasars (Ramos Almeida et al. 2022).

²Calculated using Ned Wright’s Javascript Cosmology Calculator (Wright 2006).

2 OBSERVATIONS AND DATA REDUCTION

F13451+1232 was observed in Band 3 of ALMA on two dates using different configurations of the 12 m array (Project Code 2019.1.01757.S): the array configuration used on the 2021 September 10 (baselines = 180–16200 m) resulted in a beam size of 0.083×0.069 arcsec, while the configuration used on the 2021 September 28 (baselines = 70–14400 m) resulted in a beam size 0.166×0.123 arcsec. The total time on-source was 5588 s (~ 1.5 h). Four spectral windows were used for the observations: one centred on 102.790 GHz with a bandwidth of 1.875 GHz (covering the CO(1–0) line), and the remaining three centred on 104.581, 90.977, and 92.477 GHz with bandwidths of 2.000 GHz (covering the continuum). J1337–1257 and J1353+1435 were observed to provide bandpass/flux and phase calibration, respectively; phase self-calibration was performed using the MIRIAD data reduction package (Sault, Teuben & Wright 1995).

The CO(1–0) transition was targeted for two reasons. First, the ALMA observing band that includes the CO(1–0) line covers a wider range in velocity than those that include higher order transitions such as CO(2–1) or CO(3–2), and therefore facilitates more accurate continuum subtraction. Second, the CO(1–0) transition is less susceptible to gas excitation conditions than the higher order CO transitions, and hence may be a more reliable probe of molecular gas masses in ULIRGs.

In order to check for instrumental errors such as bandpass and spectral calibration issues, we produced three CO(1–0) line datacubes: two produced using the visibilities of the two different array configurations separately, and one produced by combining the visibilities from both observations (with a final beam size of 0.113×0.091 arcsec, PA = -51.8°). To optimize the column density sensitivity, and to ensure that the dirty beam was not significantly non-Gaussian, each CO(1–0) line cube was made using Briggs weighting with robust = 1. When inspecting these cubes individually, we did not find any indications of bandpass or spectral calibration issues.

The data products produced by the automated ALMA pipeline are potentially affected by issues related to continuum subtraction, which are a consequence of the bright and steep continuum emission produced by the primary nucleus of F13451+1232. Therefore, for all three datacubes, we started with the respective visibilities as calibrated by the ALMA pipeline and applied a standard self-calibration using continuum images made from the line-free channels. We then created the line datacubes, and removed the continuum in each by subtracting a linear function that was fitted to the continuum on either side of (but excluding) the CO(1–0) emission. A continuum image was also generated from the combined visibilities of both observations using the continuum spectral windows. We used least-squares fitting with the ASTROPY (Astropy Collaboration 2013, 2018) PYTHON module to fit a two-dimensional Gaussian to the point source in this continuum image, and took the centroid position (13:47:33.36 +12 17 24.23) to be the location of the nucleus. The continuum image was made using uniform weighting and has a resolution of 0.049×0.033 arcsec (PA = -46.8°).

To ensure the highest sensitivity and signal to noise, we henceforth only consider the combined CO(1–0) datacube in our main analysis, which was produced using the combined visibilities of both observations; we discuss results from the cubes produced using the two observations separately in Appendix B. The combined cube has a root-mean-square (RMS) noise of $0.148 \text{ mJy beam}^{-1}$ for a velocity resolution of 28.8 km s^{-1} .

3 ANALYSIS AND RESULTS

3.1 Moment maps

To investigate the flux and kinematic structures of the CO(1–0) emission around the primary nucleus of F13451+1232, we first created moment maps of the combined datacube using the SOFIA-2 source-finding pipeline (Serra et al. 2015; Westmeier et al. 2021). First, SOFIA-2 applied different combinations of spatial and velocity smoothing to the datacube: Gaussian filters with full width at half-maximums of 0, 3, 6, 12, and 15 pixels were used for the spatial smoothing, and boxcar filters of widths 0, 3, 7, and 15 channels were used for the velocity smoothing. For each combination of spatial and velocity smoothing, emission above $4\sigma_{\text{rms}}$ was added to a total mask. This mask was then applied to the original, non-smoothed datacube, from which the maps in Figs 1 and 2 were produced.

In the 6×6 kpc moment maps (Fig. 1), cold molecular gas is detected to radial distances of ~ 2.5 arcsec (~ 5.5 kpc) south of the primary nucleus, and ~ 1 arcsec (~ 2 kpc) to the west. This large-scale ($r > 1$ kpc) emission, which has velocities in redshift and blueshift of up to $|v| \sim 500$ km s $^{-1}$, is indicative of gas that has been disturbed by the merger.

Within the central kiloparsec of the primary nucleus (Fig. 2), there is clear evidence for a disc with radius $r_{\text{disc}} \sim 0.5$ kpc centred on the nucleus, blueshifted to the east and redshifted to the west, with a projected maximum flux-weighted velocity of 200–250 km s $^{-1}$. In addition, there is an extended region (up to $r \sim 0.3$ arcsec or 660 pc from the nucleus along PA = 120°) of emission with higher velocity dispersions ($\sigma > 150$ km s $^{-1}$) than that of the disc. Furthermore, a particularly prominent redshifted component with a velocity dispersion of ~ 250 km s $^{-1}$ is seen within ~ 0.1 arcsec (~ 220 pc) of the continuum centre.

3.2 Properties of the kpc-scale disc

To separate non-gravitational kinematics from those expected from a rotating gas disc, we modelled the disc using the 3DFIT task from the BBAROLO tool (Di Teodoro & Fraternali 2015); the fitting process and results are detailed in Appendix A. From the BBAROLO model, we find that the disc has an average inclination of $i \approx 54^\circ$ (where $i = 0^\circ$ corresponds to the disc being face-on) and that its major axis lies along PA $\approx 248^\circ$. The deprojected rotational velocity increases from $v_{\text{rot}} = 246$ km s $^{-1}$ to $v_{\text{rot}} = 307$ km s $^{-1}$ over the radius range 28 pc $< r_{\text{disc}} < 560$ pc. We highlight that the purpose of this modelling was solely to give a reasonable estimate of the maximum rotational velocity of the molecular gas, which was needed to robustly identify non-rotational motions in our analysis. Considering this, it is notable that the high velocity-dispersion emission ($\sigma > 150$ km s $^{-1}$) seen near the disc in the moment maps (Fig. 2) cannot be accounted for by the BBAROLO model (see Fig. A1), and thus cannot be explained as being part of the rotating gas disc.

3.3 Kinematics of the non-rotating gas

To investigate the non-rotational kinematics further, we binned the velocity channels of the original cube by a factor of three and applied Hanning smoothing using the CASA software suite (CASA Team et al. 2022) to improve the signal-to-noise ratio of the emission. This resulted in a cube of velocity resolution of 86.4 km s $^{-1}$, with an RMS noise of 0.083 mJy beam $^{-1}$. Using the PVEXTRACTOR PYTHON

module,³ we extracted 1.00×0.05 arcsec slices, centred on the nucleus, from both this datacube and the BBAROLO disc-model datacube along the major axis of the disc (PA = 248°) and in the direction of the high-velocity dispersion gas near the nucleus (PA = 120°). From these slices, we produced position-velocity (PV) diagrams, which we present in Fig. 3. In the PV diagrams, there is clear evidence for non-rotational kinematics, with detected velocities being well above the projected maximum rotational disc velocity given by the BBAROLO model. There is intermediate-velocity emission ($300 < |v| < 400$ km s $^{-1}$) seen in both blueshift and redshift along PA = 120°, in the ranges $0.1 < r < 0.3$ arcsec and $0.0 < r < 0.2$ arcsec, respectively, to the southeast (SE) of the nucleus. Moreover, the compact ($r < 0.1$ arcseconds) redshifted feature visible in the moment maps (Fig. 2) can be seen in the PV diagrams between $400 < v < 680$ km s $^{-1}$, located close to the nucleus.

3.4 Comparison to the small-scale radio structure

Due to the velocities at which the compact, high-velocity nuclear feature is detected, it is unambiguously distinct from the rotating gas disc: it may be interpreted as either an inflow moving towards the nucleus on the observer’s side of the disc, or an outflow originating from the nucleus on the far side of the disc. Spatial comparison of the high-velocity flow to the small-scale radio structure may provide an indication of the nature of this flowing gas and, if it is an outflow, the driving mechanism. In Fig. 4(a), we show the flux map integrated over the range $400 < v < 680$ km s $^{-1}$ — in which we detect peak emission above the $6\sigma_{\text{rms}}$ level — along with very long baseline interferometry (VLBI) 1266 MHz continuum imaging (from global VLBI experiment GM62B; data presented and detailed in Morganti et al. 2013) of the central 0.20×0.20 arcsec (440×440 pc). The beam size of the VLBI observations was 8.01×4.89 mas (PA = -20.2°). Due to the small uncertainties in the ALMA pointing, the VLBI image was offset from our continuum centre by ~ 0.1 arcsec. We accounted for this pointing error by aligning the compact core seen in the VLBI image with the continuum centre, as it is expected that the same source is being imaged at different spatial resolutions.

By fitting a 2D Gaussian profile to the integrated high-velocity CO(1–0) emission in Fig. 4(a) using the EMCEE Python module (Foreman-Mackey et al. 2013), we find it to be offset to the SE of the continuum centroid by $(3.2 \pm 0.2) \times 10^{-2}$ arcsec (70 ± 4 pc) along PA $\sim 155^\circ$. We highlight that this is within the spatial extent of, and has a similar PA to, the small-scale radio structure ($r \sim 0.07$ arcsec; PA = 151°)

3.5 Channel maps

To determine the level at which the high-velocity, nuclear CO(1–0) emission is detected in different velocity channels, we created channel maps of the central kiloparsec of the primary nucleus from the 86.4 km s $^{-1}$ velocity resolution cube. The high-velocity ($400 < v < 600$ km s $^{-1}$) channel maps — presented in Fig. 5 — show emission above the $3\sigma_{\text{rms}}$ level (and up to $4\sigma_{\text{rms}}$) in all four channels on scales similar to that of the beam size (0.11 arcsec or 240 pc), indicating that the feature is spatially unresolved in the combined datacube.

³<https://pvextractor.readthedocs.io/en/latest/>

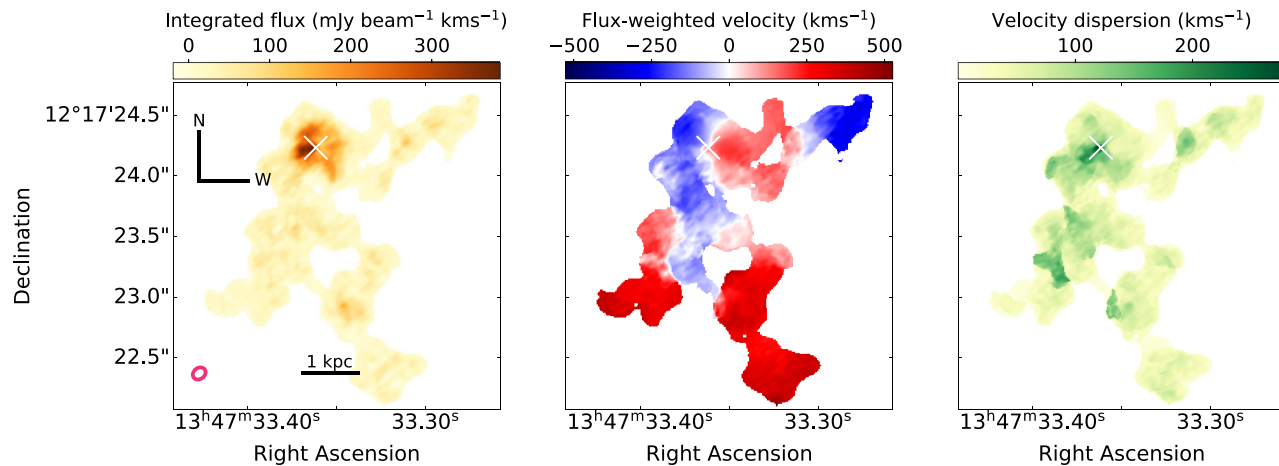


Figure 1. Integrated flux (moment 0), flux-weighted velocity (moment 1), and velocity dispersion (moment 2) maps for the central ~ 6 kpc of the primary nucleus of F13451+1232. The white cross marks the continuum centre, which we take to be the position of the AGN nucleus. The beam size of the observations is shown as a pink ellipse in the bottom left corner, and a 1 kpc scale bar is shown in black.

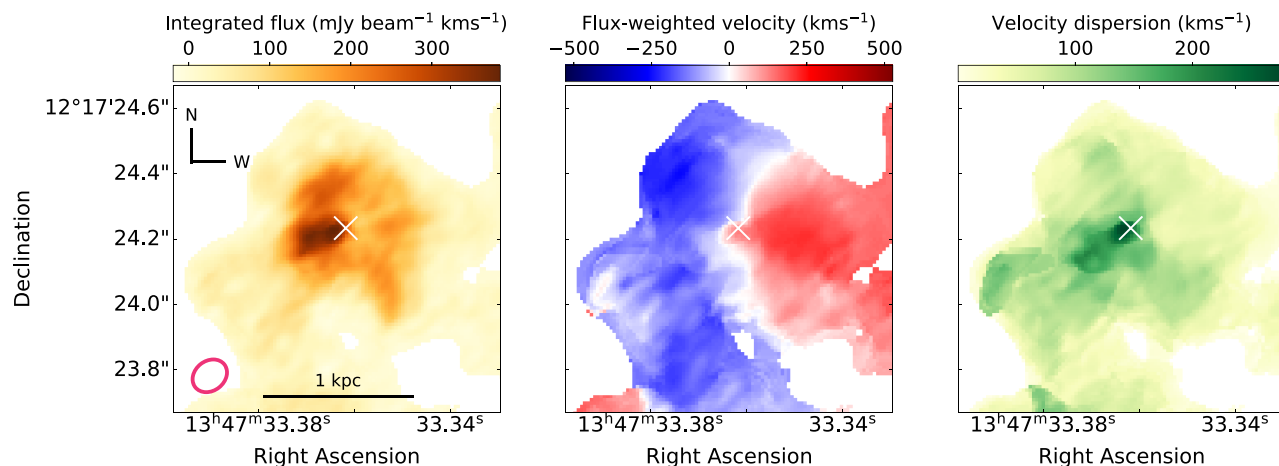


Figure 2. Integrated flux (moment 0), flux-weighted velocity (moment 1), and velocity dispersion (moment 2) maps for the inner kiloparsec region of the primary nucleus of F13451+1232; the marker and symbol scheme is the same as in Fig. 1.

3.6 Potential effects of continuum subtraction

Due to the bright, steep-spectrum continuum around the CO(1–0) line – originating from primary nucleus of F13451+1232 (as seen in the cores of other compact steep-spectrum (CSS) and GPS sources, e.g. Oosterloo et al. 2019) – it is possible that inaccuracies in the continuum subtraction process have contributed flux to the compact, redshifted, high-velocity feature that is detected at the position of the nucleus. However, we argue that this feature represents real CO(1–0) emission, for several reasons. First, the flux is detected above the 6σ level in the flux map integrated over the velocity range $400 < v < 680 \text{ km s}^{-1}$ (Fig. 4a), and in multiple velocity channels at the $3\text{--}4\sigma_{\text{rms}}$ levels (Fig. 5). Secondly, it has a significantly higher flux than the negative or positive residual features detected in the integrated spectrum (Fig. 4b). Finally, and most importantly, the feature is detected at the same velocity – and at higher flux than any residual features – in both of the two observations that were used to produce the combined datacube, despite their differing spatial resolutions (see Appendix B). While we cannot entirely rule out some contribution from instrumental effects, we conclude that this feature is real.

It is notable that previous CO(2–1) observations of the primary nucleus of F13451+1232 – that were of similar sensitivity to our CO(1–0) observations – did not detect evidence for nuclear outflows (Lamperti et al. 2022). However, in those observations, the other spectral windows were also used when fitting a linear slope to the continuum because of the narrower observing band (a factor of two narrower in velocity) of CO(2–1) observations relative to CO(1–0) – this may have led to oversubtraction of the high-velocity outflow component. Therefore, it is possible that outflow emission in CO(2–1) was not detected due to uncertainties in the continuum subtraction process.

3.7 Outflow energetics

In order to provide an estimate of the mass inflow/outflow rates of the high-velocity, spatially-unresolved redshifted feature located at the position of the nucleus, we extracted an elliptical aperture matching the beam size (0.113×0.091 arcsec, PA = -51.8° ; shown in Fig. 4a) from the datacube. We then summed all pixels within the aperture to create a line profile, which we present in Fig. 4b, and selected

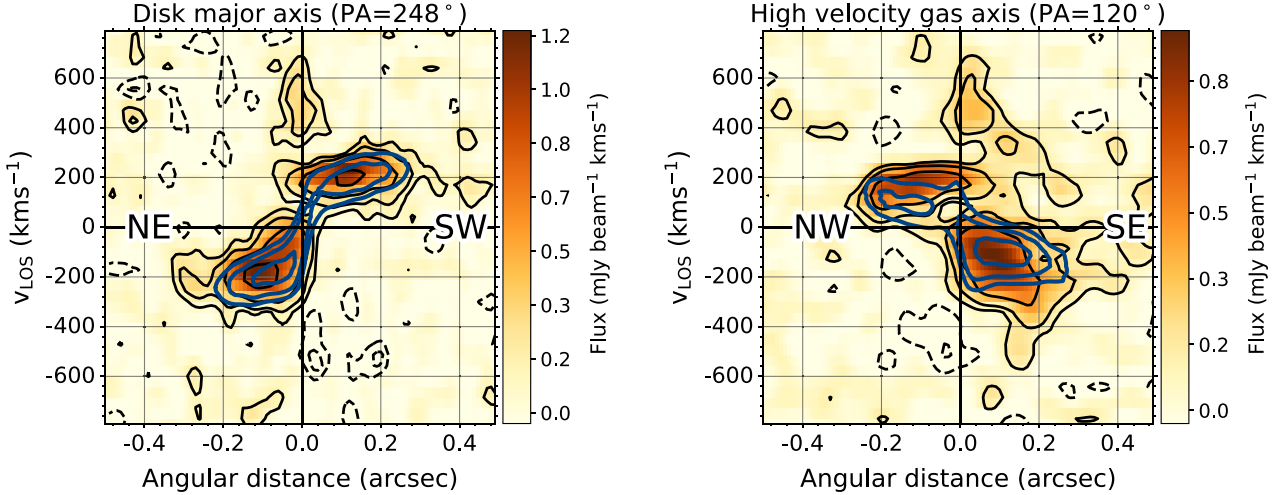


Figure 3. Position-velocity (PV) diagrams for 1.00×0.05 arcsec slices with PA = 248° (left; the major axis of the disc) and PA = 120° (right; the direction of the high-velocity dispersion emission seen in Fig. 2), centred on the continuum centre. CO(1–0) emission is shown in yellow/orange, with black contours at the $-3\sigma_{\text{rms}}$, $-1.5\sigma_{\text{rms}}$, $1.5\sigma_{\text{rms}}$, $3\sigma_{\text{rms}}$, $6\sigma_{\text{rms}}$, and $12\sigma_{\text{rms}}$ levels (dashed: negative; solid: positive); solid blue contours show the flux from the BBAROLO disc model at the same σ_{rms} levels. Extended, intermediate-velocity emission is seen in both redshift and blueshift in the PA = 120° diagram, and a compact, higher velocity feature ($400 < v < 680 \text{ km s}^{-1}$) centred approximately on the nucleus (0.0 arcsec) can clearly be seen in both diagrams.

emission between $400 < v < 680 \text{ km s}^{-1}$ to isolate the non-rotating gas.

For the extended, intermediate-velocity ($300 < |v| < 400 \text{ km s}^{-1}$) emission seen in blueshift and redshift, we extracted two subapertures from the 1.00×0.05 arcsec slice along PA = 120° (used to create the right PV diagram in Fig. 3): one covering radii $0.0 < r < 0.2$ arcsec (for the extended redshifted emission), and the other covering the range $0.1 < r < 0.3$ arcsec (for the extended blueshifted emission). We then selected emission between $300 < v < 400 \text{ km s}^{-1}$ and $-400 < v < -300 \text{ km s}^{-1}$, respectively, in these slices to isolate the non-rotating gas.

For every channel within the range of the selected velocities in the extracted apertures, we calculated CO(1–0) fluxes ($S_{\text{CO}}\Delta V$) and converted them to luminosities (L_{CO}) using the relation presented by Solomon & Vanden Bout (2005):

$$L_{\text{CO}}^{\prime} = 3.25 \times 10^7 S_{\text{CO}}\Delta V v_{\text{obs}}^{-2} D_L^2 (1+z)^{-3}, \quad (1)$$

where v_{obs} is the observed frequency of the CO(1–0) line (102.789 GHz) and D_L is the luminosity distance to F13451+1232. We then summed the CO(1–0) luminosities across all selected velocity channels, resulting in total luminosities for each of the two intermediate-velocity features and the high-velocity feature. Assuming a CO-to- H_2 conversion factor of $\alpha_{\text{CO}} = 0.8 M_{\odot} (\text{K km s}^{-1} \text{pc}^2)^{-1}$ (typical for ULIRGs: Downes & Solomon 1998), we converted these total luminosities into molecular gas masses. We also applied this method to the rotating kpc-scale CO disc, for which we estimate a total mass of $1.1 \times 10^{10} M_{\odot}$.

The corresponding mass flow rates of the non-rotating molecular gas were estimated using

$$\dot{M}_{\text{flow}} = \frac{M_{\text{flow}} v_w}{\Delta R} \cdot \tan\theta, \quad (2)$$

where v_w is the flux-weighted velocity, ΔR is the range in radius covered by the flow, and θ is the angle of the flow relative to our line of sight. The $\tan\theta$ term is required to correct for projection effects in both radius and velocity. To estimate this projection factor, we assumed a solid-angle-weighted mean inclination for random orientations of the line of sight to the outflow direction, giving $\theta =$

57.3° . Finally, we estimated kinetic powers with

$$\dot{E}_{\text{kin}} = \frac{1}{2} \dot{M}_{\text{flow}} \left(\frac{v_w}{\cos\theta} \right)^2. \quad (3)$$

We present the resulting CO(1–0) luminosities, masses, flux-weighted velocities, flow radii, mass flow rates, kinetic powers, and coupling efficiencies ($\epsilon_f = \dot{E}_{\text{kin}}/L_{\text{bol}}$) in Table 1. For the high-velocity nuclear gas, we derive a mass flow rate of $\dot{M}_{\text{out}} \sim 230 M_{\odot} \text{ yr}^{-1}$, which corresponds to a kinetic power that is ~ 1.4 per cent of the bolometric luminosity of the AGN ($L_{\text{bol}} = 4.8 \times 10^{45} \text{ erg s}^{-1}$; Rose et al. 2018). In contrast, we find much lower mass flow rates ($\dot{M}_{\text{out}} = 22\text{--}27 M_{\odot} \text{ yr}^{-1}$) and kinetic powers ($(6.0\text{--}7.1) \times 10^{-2}$ per cent of L_{bol}) for the extended, intermediate-velocity emission.

4 DISCUSSION

In addition to a kpc-scale disc, we have detected non-rotating cold molecular gas in CO(1–0) emission near the primary nucleus of F13451+1232. This non-rotating gas consists of spatially extended ($0.0 < r < 0.3$ arcsec; $0 < r < 660$ pc), intermediate-velocity ($300 < |v| < 400 \text{ km s}^{-1}$) components seen in both blueshift and redshift, and a compact ($r < 0.06$ arcsec; $r < 120$ pc), spatially unresolved, high-velocity ($400 < v < 680 \text{ km s}^{-1}$) nuclear component seen in redshift.

4.1 Interpreting the non-rotating gas as inflowing

Given that the AGN in F13451+1232 may have recently restarted and thus be young (Stanghellini et al. 2005; Morganti et al. 2013), if the non-rotating gas seen in intermediate- and high-velocity CO(1–0) emission is inflowing, it is possible that we are directly observing the gas flows responsible for its triggering. The total gas flow rates ($27\text{--}230 M_{\odot} \text{ yr}^{-1}$; Table 1) are orders of magnitude higher than those needed to sustain the AGN ($0.8 M_{\odot} \text{ yr}^{-1}$, assuming $\eta = 0.1$ and $L_{\text{bol}} = 4.8 \times 10^{45} \text{ erg s}^{-1}$; Rose et al. 2018). Therefore, this is a plausible feeding mechanism even if only a small fraction of the inflowing gas is accreted on to the central supermassive black hole. However, we argue below that the compact, high-velocity component

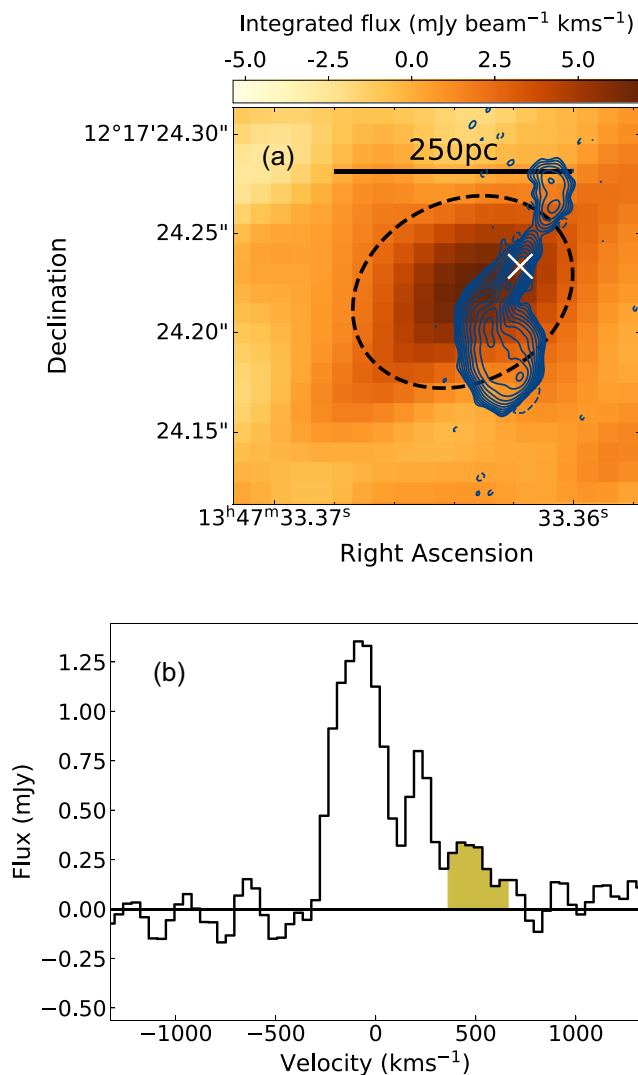


Figure 4. (a) Integrated flux map (orange–brown) of the velocity channels between $400 < v < 680 \text{ km s}^{-1}$. The dashed black ellipse shows the aperture extracted from the datacube to derive the mass of the outflow; the corresponding line profile is shown in Fig. 4(b). The small-scale radio structure, as seen in VLBI 1266 MHz continuum imaging (Morganti et al. 2013), is shown as dark blue solid contours at the $0.3 \times (-1, 1, 2, 4, 8, 16, 32, 64, 128, 256, 512, 1024) \text{ mJy beam}^{-1}$ levels, whereas the white cross marks the position of the continuum centre seen in our observations (Section 2). (b) CO(1–0) line profile extracted from the aperture that covers the outflow; the line profile shown was extracted from the 84 km s^{-1} velocity resolution combined datacube. The part of the line profile that we take to represent in-/out-flowing gas ($400 < v < 680 \text{ km s}^{-1}$) is shaded in yellow.

(and potentially also the intermediate-velocity emission) is in reality outflowing, rather than inflowing.

4.2 The spatially extended, intermediate-velocity gas

The nature of the intermediate-velocity emission ($300 < |v| < 400 \text{ km s}^{-1}$) that is seen in both redshift and blueshift in the PV diagram along $\text{PA} = 120^\circ$ (Fig. 3) – and as a region of higher velocity dispersion to the SE of the nucleus in the moment 2 maps (Figs 1 and 2) – is not clear. On one hand, it may represent spatially extended ($220 < r < 440 \text{ pc}$) AGN-driven outflows. However, since

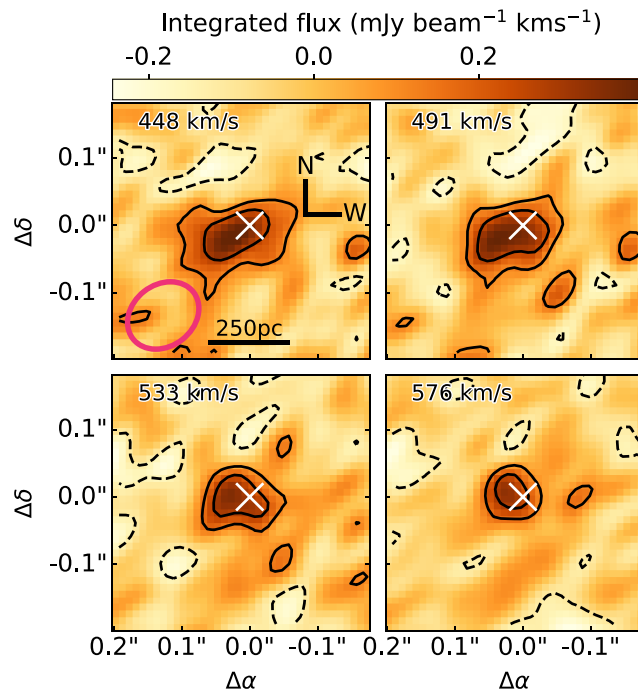


Figure 5. Channel maps of the central $\sim 1 \text{ kpc}$ of the primary nucleus of F13451+1232 (centred on the nucleus: Section 2) between $448 < v < 576 \text{ km s}^{-1}$, taken from the velocity-binned and smoothed cube with channel widths of 43.7 km s^{-1} and a velocity resolution of 86.4 km s^{-1} . Black contours are shown at the $-3\sigma_{\text{rms}}, -1.5\sigma_{\text{rms}}, 1.5\sigma_{\text{rms}}, 3\sigma_{\text{rms}}$ levels (dashed: negative; solid: positive), where σ_{rms} is the RMS of the binned-and-smoothed cube. The continuum centre is marked as a white cross in each channel; the beam size is shown as a pink ellipse in the 448 km s^{-1} channel map (top left panel).

the emission extends well beyond the compact radio source, then these outflows would not be driven solely by the jet – an additional outflow driving mechanism would be required. Based on the similar PAs of the extended emission and the small-scale radio structure, one possibility is that this gas is accelerated by radiatively-driven winds that are collimated by a circumnuclear torus with an axis similar to that of the compact radio source. Alternatively, due to the velocities not being much above those expected for rotation (as given by the BBAROLO MODEL: Section 3.2), this extended emission may represent material from the merger settling on to the disc. This latter interpretation is supported by the larger-scale ($r > 1 \text{ kpc}$) filament-like structures seen to the south and west of the primary nucleus (Fig. 1), which likely represent gas disturbed by the merger: these large-scale structures have similar velocity shifts and dispersions to the intermediate-velocity gas seen near the nucleus.

If the intermediate-velocity emission truly did represent AGN-driven outflows, then its mass outflow rates ($22\text{--}27 M_\odot \text{ yr}^{-1}$) are higher than those of the previously detected warm ionized ($11.3 M_\odot \text{ yr}^{-1}$: Rose et al. 2018)⁴ and neutral H I ($\sim 6 M_\odot \text{ yr}^{-1}$)⁵

⁴The warm ionized mass outflow rates and kinetic powers were calculated following the second method of Rose et al. (2018), which involves using the v_{05} parameter as the outflow velocity to account for projection effects; these estimates are likely to be upper limits.

⁵The neutral H I mass outflow rate has been recalculated using the methodology in appendix C1 of Holden et al. (2023) with the values presented by Morganti et al. (2013); the kinetic power and coupling efficiency have been

Table 1. CO(1–0) luminosities, masses, projected flux-weighted velocities, aperture radii, projected mass flow rates ($\dot{M}_{\text{flow,proj}}$), deprojected mass flow rates (\dot{M}_{flow}), and deprojected energetics for the extended emission in both blueshift and redshift, and the nuclear redshifted feature seen in the PV diagrams (Fig. 3). When deprojecting, we assumed $\theta = 57.3^\circ$ (see Section 3.7).

Component	L'_{CO} ($\text{K km s}^{-1} \text{pc}^2$)	M_{flow} (M_\odot)	v_w (km s^{-1})	ΔR^a (arcsec)	$\dot{M}_{\text{flow,proj}}$ ($M_\odot \text{yr}^{-1}$)	\dot{M}_{flow} ($M_\odot \text{yr}^{-1}$)	\dot{E}_{kin} (erg s^{-1})	ϵ_f^b (per cent)
Extended blueshifted	2.7×10^7	2.2×10^7	−339	0.2	17	27	3.4×10^{42}	7.1×10^{-2}
Extended redshifted	2.2×10^7	1.8×10^7	350	0.2	14	22	2.9×10^{42}	6.0×10^{-2}
Nuclear redshifted	4.2×10^7	3.4×10^7	514	0.0545	148	230	6.6×10^{43}	1.4

^aFor the extended emission, we take ΔR to be the radial distance over which the extended emission is seen; for the spatially unresolved, high-velocity redshift feature, we take ΔR to be half of the beam major axis.

^bCalculated assuming $L_{\text{bol}} = 4.8 \times 10^{45} \text{ erg s}^{-1}$ (Rose et al. 2018).

phases. Furthermore, they are similar to those recently reported for the cold molecular outflows in a sample of nearby QSO2s ($8\text{--}16 M_\odot \text{yr}^{-1}$; Ramos Almeida et al. 2022), which were identified using a similar method to that used here for the intermediate-velocity gas. When applying a factor of three to account for assumed spherical outflow geometry, as was done by Fiore et al. (2017), we find (in agreement with Ramos Almeida et al. 2022) that these mass outflow rates ($66\text{--}81 M_\odot \text{yr}^{-1}$) fall significantly below the correlation between mass outflow rate and AGN bolometric luminosity given by Fiore et al. (2017). However, it is important to note that Lamperti et al. (2022) reported a wide range of mass outflow rates for ULIRGs with similar bolometric luminosities ($6 < \dot{M}_{\text{flow}} < 300 M_\odot \text{yr}^{-1}$), indicating that the high-mass outflow rates found by Fiore et al. (2017) may represent the most extreme cases, and therefore represent the upper envelope to any relationship between mass outflow rate and AGN bolometric luminosity (see also Speranza et al. 2024).

4.3 The compact, high-velocity nuclear outflow

While it is possible that the intermediate-velocity emission does not represent outflowing gas, we highlight that the observed velocities of the redshifted nuclear feature ($400 < v < 680 \text{ km s}^{-1}$) are much higher than what would be expected due to settled gravitational motions ($v < 300 \text{ km s}^{-1}$: the projected velocities seen in the disc). Moreover, the emission of this component is compact ($r < 120 \text{ pc}$), unresolved in the combined datacube, and on a similar radial scale to both the compact radio structure ($r < 0.06 \text{ arcsec}$; $r < 130 \text{ pc}$; Fig. 4a) and the other outflow phases ($r < 100 \text{ pc}$; Morganti et al. 2013; Tadhunter et al. 2018). Therefore, it is much more likely that we are seeing a nuclear outflow, rather than an inflow or settling gas from the merger. Furthermore, the fact that the high-velocity emission is spatially offset from the nucleus (by $(3.2 \pm 0.2) \times 10^{-2} \text{ arcsec}$) along a direction that is close to that of the small-scale radio structure (PA = 151°) suggests a relation between the two. This is consistent with acceleration by shocks, which may be induced by either a jet or a broader, radiatively driven wind that is collimated by the circumnuclear torus. Given that the compact CO(1–0) outflow is seen to be offset along the direction of the radio structure (which would not necessarily be expected in the radiatively driven scenario), and that the neutral atomic outflow component (detected in H I absorption) is seen to be coincident with the radio hotspot (Morganti et al. 2013), we favour the jet-driven interpretation. In this context, it is interesting to note the Southern bend in the small-scale radio structure, which may be due to the jet colliding with dense molecular gas, being deflected, and thereby launching the nuclear outflow.

recalculated by using these values with equation (3) and assuming $L_{\text{bol}} = 4.8 \times 10^{45} \text{ erg s}^{-1}$ (Rose et al. 2018).

The cold molecular mass outflow rate for this nuclear component ($\dot{M}_{\text{flow}} \sim 230 M_\odot \text{yr}^{-1}$) is more than an order of magnitude higher than those previously derived for the other outflow phases in F13451+1232, lies within the range of values for molecular outflows previously detected in ULIRGs (a few to thousands of solar masses per year; Cicone et al. 2014; Pereira-Santaella et al. 2018; Fluetsch et al. 2019; Herrera-Camus et al. 2020; Lamperti et al. 2022), and is close to (within 1σ of) the correlation between cold molecular mass outflow rate and AGN bolometric luminosity found by Fiore et al. (2017) when corrected for assumed spherical outflow geometry.

Overall, the kinetic power of the cold molecular phase in F13451+1232 ($6.6 \times 10^{43} \text{ erg s}^{-1}$) accounts for ~ 1.4 per cent of L_{bol} – approximately a factor of three higher than the combined kinetic power of the neutral H I (~ 0.04 per cent of L_{bol} ; Morganti et al. 2013) and warm ionized (0.49 per cent of L_{bol} ; Rose et al. 2018) outflow phases. Therefore, for all phases, the *total* outflow kinetic power is ~ 2 per cent of the AGN bolometric luminosity. While this is consistent with the requirements of simulations of outflows launched by AGN in galaxy mergers ($0.5 < \epsilon_f < 10$ per cent: e.g. Di Matteo et al. 2005; Hopkins & Elvis 2010) – and thus may be interpreted as the outflows having an impact on the evolution of the galaxy – we highlight that such comparisons must be done with care, and that it is unclear if such interpretations can be made robustly (see Harrison et al. 2018).

Finally, we emphasize that even if we assume a CO-to-H₂ conversion factor that is at the lower end of the range of values used in the literature (i.e. $\alpha_{\text{CO}} = 0.3 M_\odot (\text{K km s}^{-1} \text{pc}^2)^{-1}$ for optically thin gas; Oosterloo et al. 2017, 2019), the derived cold molecular, nuclear mass outflow rate is still much higher than those of the other phases ($\sim 86 M_\odot \text{yr}^{-1}$). Conversely, if a conversion factor that is characteristic of molecular clouds in the Milky Way is assumed ($\alpha_{\text{CO}} = 4.3 M_\odot (\text{K km s}^{-1} \text{pc}^2)^{-1}$; Bolatto, Wolfire & Leroy 2013), the mass and kinetic power of this outflow increase significantly ($\dot{M}_{\text{out}} \sim 1240 M_\odot \text{yr}^{-1}$; $\epsilon_f \sim 7$ per cent).

5 CONCLUSIONS

Through the analysis of high-spatial resolution CO(1–0) observations of the primary nucleus of the ULIRG F13451+1232, we have detected and characterized a kpc-scale circumnuclear disc and spatially extended ($0.0 < r < 0.3 \text{ arcsec}$; $0 < r < 660 \text{ pc}$), intermediate-velocity emission ($300 < |v| < 400 \text{ km s}^{-1}$). This intermediate-velocity molecular gas may represent AGN radiation-driven outflows, or merger material settling on to the disc. Furthermore, we have also presented evidence for a compact ($r < 120 \text{ pc}$), cold molecular outflow ($400 < v < 680 \text{ km s}^{-1}$) at the position of the nucleus with a mass outflow rate of $\dot{M}_{\text{out}} \sim 230 M_\odot \text{yr}^{-1}$ and a kinetic power that is ~ 1.4 per cent of the AGN bolometric luminosity.

Overall, our detection of cold molecular outflow(s) in F13451+1232 changes the scenario of the AGN-driven outflows in this object: previous studies found that the neutral atomic HI and warm ionized phases had relatively modest mass outflow rates, whereas here we find that the cold molecular outflow is carrying over an order of magnitude more mass (and several times the kinetic power) than the warm ionized and neutral phases. Similar results have been found for other types of active galaxy, where the colder phases have been seen to carry the majority of the outflowing mass (Ramos Almeida et al. 2019; Holden & Tadhunter 2023; Holden et al. 2023; Speranza et al. 2024). This further demonstrates the need for multiwavelength observations to fully quantify the impact of AGN-driven outflows. Moreover, a similarly compact ($r < 120$ pc) but more massive ($\dot{M}_{\text{out}} \sim 650 M_{\odot} \text{yr}^{-1}$) outflow was found in the ULIRG PKS 1549–79 (Oosterloo et al. 2019), which is also both a merger and a luminous radio source. Our results thus provide important evidence that such powerful radio sources accelerate compact molecular outflows, and that these outflows may carry more mass and power than other gas phases.

Crucially, in demonstrating that cold molecular AGN-driven outflows can be compact ($r < 120$ pc), our study emphasizes the importance of high-spatial resolution observations when robustly quantifying the impact of AGN-driven outflows on their host galaxies.

ACKNOWLEDGEMENTS

We thank the anonymous referee for their feedback, which helped to improve the quality of this manuscript. LRH and CNT acknowledge support from STFC, grant code ST/V507040/1. This paper makes use of the following ALMA data: ADS/JAO.ALMA#2019.1.01757.S. ALMA is a partnership of ESO (representing its member states), NSF (USA), and NINS (Japan), together with NRC (Canada), MOST and ASIAA (Taiwan), and KASI (Republic of Korea), in cooperation with the Republic of Chile. The Joint ALMA Observatory is operated by ESO, AUI/NRAO, and NAOJ. The European VLBI Network is a joint facility of independent European, African, Asian, and North American radio astronomy institutes. Scientific results from data presented in this publication are derived from the following EVN project code(s): GM062. AA and CRA acknowledge the projects “Feeding and feedback in active galaxies”, with reference PID2019-106027GB-C42, funded by MICINN-AEI/10.13039/501100011033, and “Quantifying the impact of quasar feedback on galaxy evolution”, with reference EUR2020-112266, funded by MICINN-AEI/10.13039/501100011033 and the European Union NextGenerationEU/PRTR. MP-S acknowledges funding support from the Ramón y Cajal programme of the Spanish Ministerio de Ciencia e Innovación (RYC2021-033094-I). IL acknowledges support from PID2022-140483NB-C22 funded by AEI 10.13039/501100011033 and BDC 20221289 funded by MCIN by the Recovery, Transformation, and Resilience Plan from the Spanish State, and by NextGenerationEU from the European Union through the Recovery and Resilience Facility.

DATA AVAILABILITY

The ALMA CO(1–0) data used in this work is publicly available from the ALMA Science Archive (<https://almascience.eso.org/aq/>) with Project Code 2019.1.01757.S. The data used to produce the VLBI 1266 MHz continuum image presented in Fig. 4(a) is publicly available from the European VLBI Network (EVN) archive for

experiment GM062B (http://archive.jive.nl/scripts/arch.php?exp=G M062B_060605).

REFERENCES

- Alonso-Herrero A. et al., 2018, *ApJ*, 859, 144
 Astropy Collaboration, 2013, *A&A*, 558, A33
 Astropy Collaboration, 2018, *ApJ*, 156, 123
 Audibert A. et al., 2023, *A&A*, 671, L12
 Bolatto A. D., Wolfire M., Leroy A. K., 2013, *ARA&A*, 51, 207
 CASA Team et al., 2022, *PASP*, 134, 114501
 Cicone C. et al., 2014, *A&A*, 562, A21
 Davé R., Anglés-Alcázar D., Narayanan D., Li Q., Rafieferantsoa M. H., Appleby S., 2019, *MNRAS*, 486, 2827
 Di Matteo T., Springel V., Hernquist L., 2005, *Nature*, 433, 604
 Di Teodoro E. M., Fraternali F., 2015, *MNRAS*, 451, 3021
 Domínguez-Fernández A. J. et al., 2020, *A&A*, 643, A127
 Downes D., Solomon P. M., 1998, *ApJ*, 507, 615
 Fiore F. et al., 2017, *A&A*, 601, A143
 Fluetsch A. et al., 2019, *MNRAS*, 483, 4586
 Foreman-Mackey D., Hogg D. W., Lang D., Goodman J., 2013, *PASP*, 125, 306
 Fotopoulou C. M., Dasyra K. M., Combes F., Salomé P., Papachristou M., 2019, *A&A*, 629, A30
 Gilmore G., Shaw M. A., 1986, *Nature*, 321, 750
 Harrison C. M., Costa T., Tadhunter C. N., Flütsch A., Kakkad D., Perna M., Vietri G., 2018, *Nat. Astron.*, 2, 198
 Heckman T. M., Smith E. P., Baum S. A., van Breugel W. J. M., Miley G. K., Illingworth G. D., Bothun G. D., Balick B., 1986, *ApJ*, 311, 526
 Herrera-Camus R. et al., 2020, *A&A*, 635, A47
 Holden L. R., Tadhunter C. N., 2023, *MNRAS*, 524, 886
 Holden L. R., Tadhunter C. N., Morganti R., Oosterloo T., 2023, *MNRAS*, 520, 1848
 Holt J., Tadhunter C. N., Morganti R., 2003, *MNRAS*, 342, 227
 Holt J., Tadhunter C., Morganti R., Bellamy M., González Delgado R. M., Tzioumis A., Inskip K. J., 2006, *MNRAS*, 370, 1633
 Holt J., Tadhunter C. N., Morganti R., Emonts B. H. C., 2011, *MNRAS*, 410, 1527
 Hopkins P. F., Elvis M., 2010, *MNRAS*, 401, 7
 Hopkins P. F., Hernquist L., Cox T. J., Kereš D., 2008, *ApJS*, 175, 356
 Kukreti P., Morganti R., Tadhunter C., Santoro F., 2023, *A&A*, 674, A198
 Lamperti I. et al., 2022, *A&A*, 668, A45
 Lister M. L., Kellermann K. I., Vermeulen R. C., Cohen M. H., Zensus J. A., Ros E., 2003, *ApJ*, 584, 135
 Magorrian J. et al., 1998, *ApJ*, 115, 2285
 Meena B. et al., 2023, *ApJ*, 943, 98
 Morganti R., Tadhunter C. N., Oosterloo T. A., 2005, *A&A*, 444, L9
 Morganti R., Fogasy J., Paragi Z., Oosterloo T., Orienti M., 2013, *Science*, 341, 1082
 Mukherjee D., Bicknell G. V., Sutherland R., Wagner A., 2016, *MNRAS*, 461, 967
 O’Dea C. P., Saikia D. J., 2021, *A&AR*, 29, 3
 Oosterloo T., Raymond Oonk J. B., Morganti R., Combes F., Dasyra K., Salomé P., Vlahakis N., Tadhunter C., 2017, *A&A*, 608, A38
 Oosterloo T., Morganti R., Tadhunter C., Raymond Oonk J. B., Bignall H. E., Tzioumis T., Reynolds C., 2019, *A&A*, 632, A66
 Pereira-Santaella M. et al., 2018, *A&A*, 616, A171
 Ramos Almeida C., Acosta-Pulido J. A., Tadhunter C. N., González-Fernández C., Cicone C., Fernández-Torreiro M., 2019, *MNRAS*, 487, L18
 Ramos Almeida C. et al., 2022, *A&A*, 658, A155
 Rose M., Tadhunter C., Ramos Almeida C., Rodríguez Zaurín J., Santoro F., Spence R., 2018, *MNRAS*, 474, 128
 Rupke D. S., Veilleux S., Sanders D. B., 2005, *ApJ*, 632, 751
 Sanders D. B., Mirabel I. F., 1996, *ARA&A*, 34, 749

- Santoro F., Rose M., Morganti R., Tadhunter C., Oosterloo T. A., Holt J., 2018, *A&A*, 617, A139
- Santoro F., Tadhunter C., Baron D., Morganti R., Holt J., 2020, *A&A*, 644, A54
- Sault R. J., Teuben P. J., Wright M. C. H., 1995, in Shaw R. A., Payne H. E., Hayes J. J. E. eds, ASP Conf. Ser. Vol. 77, *Astronomical Data Analysis Software and Systems IV*. Astron. Soc. Pac., San Francisco, p. 433
- Serra P. et al., 2015, *MNRAS*, 448, 1922
- Silk J., Rees M. J., 1998, *A&A*, 331, L1
- Solomon P. M., Vanden Bout P. A., 2005, *ARA&A*, 43, 677
- Speranza G. et al., 2024, *A&A*, 681, A63
- Stanghellini C., O’Dea C. P., Baum S. A., Dallacasa D., Fanti R., Fanti C., 1997, *A&A*, 325, 943
- Stanghellini C., O’Dea C. P., Dallacasa D., Cassaro P., Baum S. A., Fanti R., Fanti C., 2005, *A&A*, 443, 891
- Tadhunter C. et al., 2018, *MNRAS*, 478, 1558
- Villar Martín M. et al., 2023, *A&A*, 673, A25
- Westmeier T. et al., 2021, *MNRAS*, 506, 3962
- Wright E. L., 2006, *PASP*, 118, 1711

APPENDIX A: BBAROLO MODELLING OF THE GAS DISC

In order to identify non-rotational motions in the central few kiloparsecs of the primary nucleus of F13451+1232, we fit the disc-like kinematics seen in our CO(1–0) data (Section 3; Fig. 2) with a simple disc model using the 3DFIT task from the BBAROLO tool (Di Teodoro & Fraternali 2015). The 3DFIT task fits a series of concentric rings to the data in three spatial dimensions and three velocity dimensions (the rotational velocity, v_{rot} ; the radial velocity, v_{rad} , and the velocity dispersion v_{disp}).

Our fitting procedure followed the methodology outlined in Alonso-Herrero et al. (2018), Domínguez-Fernández et al. (2020), and Ramos Almeida et al. (2022). Throughout, the centre of the disc model was fixed to be the position of the continuum centre (as measured from a two-dimensional Gaussian fit to the continuum image: Section 2). We first performed an initial fit using the 3DFIT task in which the radial velocities of the rings were fixed to be 0 km s^{-1} and the scale height of the disc (z_0) was fixed to 0 pc. The remaining parameters were allowed to vary; initial values for the rotational velocity and velocity dispersion were based on the flux-weighted velocity shift and velocity dispersion maps (Fig. 2),

the initial value of the inclination ($i_{\text{initial}} = 38^\circ$) was based on the measured ratio of the projected disc major and minor axes while assuming a circular disc, and the initial value for the PA was set to that previously estimated from two-dimensional spectroastrometry of CO(2–1) observations of the disc by Lamperti et al. (2022). However, limits were imposed on the variation of these free parameters – between successive rings, the rotational velocity was not allowed to change by more than $\pm 50 \text{ km s}^{-1}$, nor were the inclination and PA allowed to change by more than $\pm 20^\circ$. The fits used uniform weighting and local normalization. It should be noted that, since the physical size of the modelled rings is much less than the beam size of the observations, the properties of adjacent rings are correlated. However, this does not have a significant effect on the maximum rotational velocity of the disc model (nor does changing the values of the initial parameters), and therefore does not affect the interpretations made in our analysis.

In order to ensure that the overall radial extent and kinematics of the disc were accurate – and to alleviate potential problems with fit degeneracy arising from having a high number of free parameters – we then used the results from the initial fit as a basis for a second fit. For this second run, we fixed the velocity dispersion, inclination, and PA to the values determined from the first run, so that only the rotational velocity was allowed to vary. We present the final model parameters for each ring in Table A1; in Fig. A1, we present the moment maps and residuals of the final disc model. High flux-weighted velocities ($\sim 200 \text{ km s}^{-1}$) and velocity dispersions ($\sigma \sim 200 \text{ km s}^{-1}$) due to non-rotational kinematics can be seen in the residual maps near the centre of the disc.

By taking an aperture around the disc in our CO(1–0) datacube and integrating between $-310 < v < 310 \text{ km s}^{-1}$, we find a disc mass of $1.1 \times 10^{10} M_\odot$ (using equation 1 and $\alpha_{\text{CO}} = 0.8 M_\odot (\text{K km s}^{-1} \text{ pc}^2)^{-1}$). Lamperti et al. (2022) also detected this nuclear disc using CO(2–1) spectroastrometry, and found a similar mass and overall properties to those reported here.

Finally, we highlight that the purpose of this modelling was solely to estimate the maximum CO(1–0) velocities that are explainable as rotational motion, and hence identify outflow kinematics; the detailed parameters of the disc model presented here are not intended to be a robust representation of the disc’s properties.

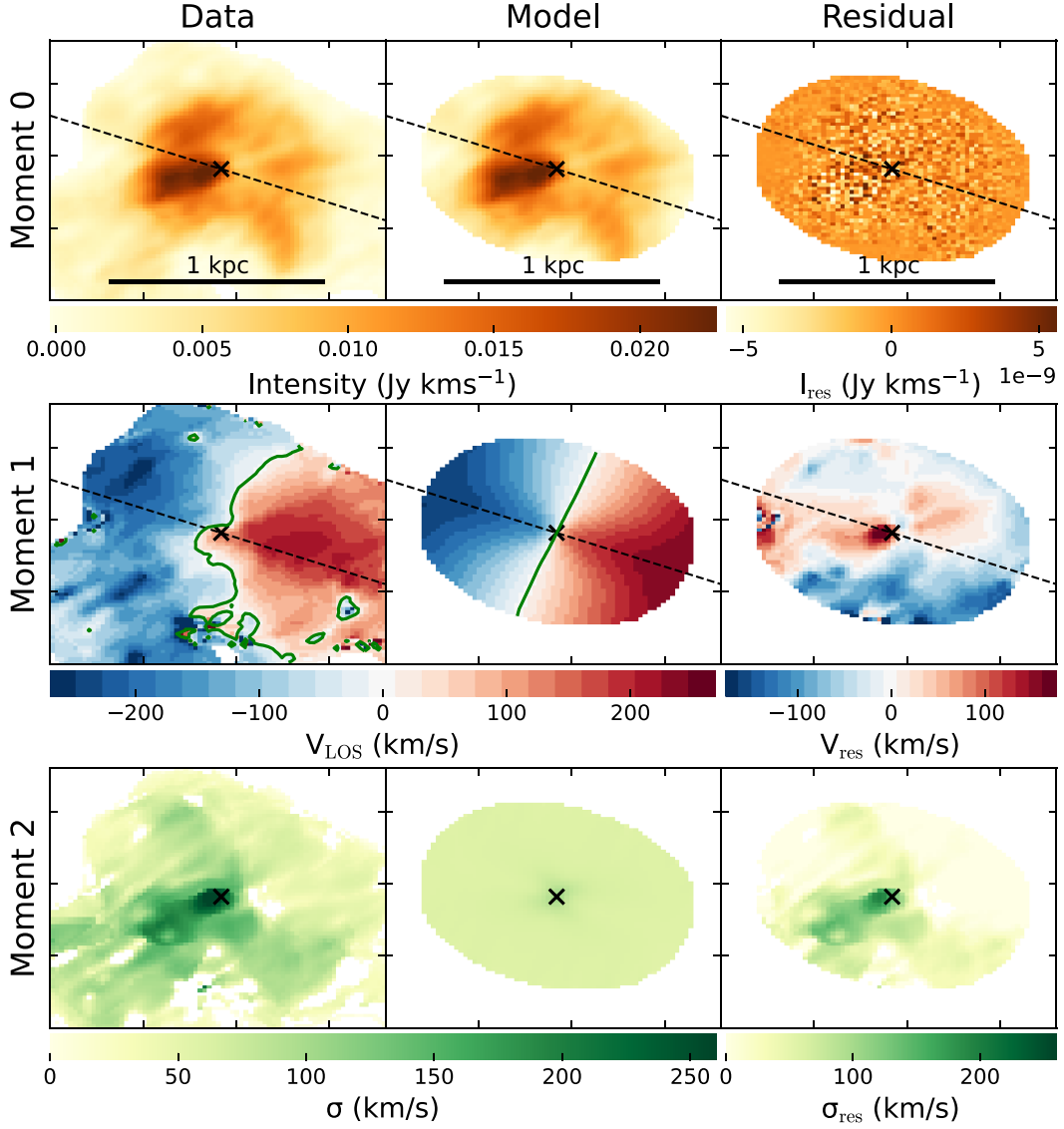


Figure A1. Integrated flux (moment 0; top), flux-weighted velocity (moment 1; middle), and velocity dispersion (moment 2; bottom) maps of the CO(1-0) data (left), BBAROLO disc model (middle), and residuals (data–model; right). The ticks have separations of 0.2 arcsec. The black dashed line shows the PA of the modelled disc, whereas the black cross shows the disc centre (which was set to be the continuum centre position; see Section 2). The solid green lines in the middle row panels are isovelocity contours at 0 km s^{-1} .

Table A1. Final parameters for each ring of the BBAROLO 3DFIT disc model. The distance of each ring to the fixed disc centre (r_{ring}) is given in both arcseconds and parsecs. Here, v_{rot} and v_{disp} are the rotational velocities and velocity dispersions of each ring, respectively.

r_{ring} (arcsec)	r_{ring} (pc)	v_{rot} (km s^{-1})	v_{disp} (km s^{-1})	i ($^{\circ}$)	PA ($^{\circ}$)
0.013	28.5	247.969	5.524	62.218	242.005
0.040	87.6	249.627	24.639	58.627	236.155
0.067	146.7	211.864	91.100	55.868	235.867
0.094	205.8	249.245	72.507	53.826	239.504
0.121	264.9	267.474	65.771	52.384	245.429
0.148	324.0	280.596	62.837	51.425	252.007
0.175	383.1	293.392	61.210	50.834	257.600
0.202	442.2	311.494	68.331	50.494	260.572
0.229	501.0	301.110	61.533	50.289	259.286
0.256	560.4	314.645	58.314	50.102	252.106

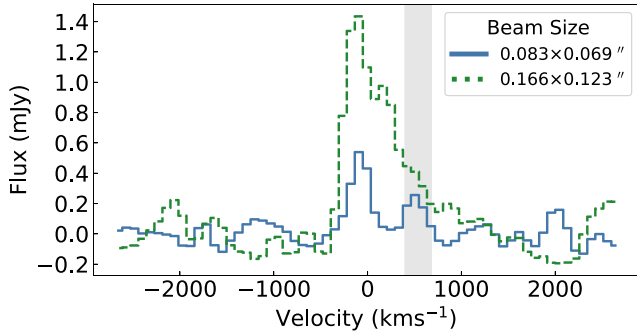


Figure B1. CO(1–0) line profiles of the primary nucleus of F13451+1232 extracted from the two sets of observations of differing array configurations (hence beam sizes) that comprise the datacube presented in our analysis (see Section 2). These profiles were extracted from the respective cubes using apertures matched to the beam sizes. It can be seen that the flux in the high-velocity redshifted component (shaded in grey) is less in the cube with the smaller beam size.

APPENDIX B: THE CO(1–0) NUCLEAR OUTFLOW OBSERVED AT DIFFERENT SPATIAL RESOLUTIONS

The CO(1–0) data that we present in this work was produced from the combined visibilities of two observations, which were taken with different array configurations and thus have different beam sizes (0.083×0.069 arcsec and 0.166×0.123 arcsec; see Section 2). Here, we discuss the detection of the high-velocity, redshifted, compact

feature seen at the position of the nucleus (Section 3; Figs 2–5) in the datacubes produced from the visibilities of these observations separately.

In Fig. B1, we present CO(1–0) line spectra extracted from these cubes; the size of the extraction aperture in each case was matched to the beam size. The high-velocity redshifted feature is well detected in both datacubes in the velocity range $400 < v < 680$ km s^{−1}, while any residual features of comparable flux are not present in both cubes at the same velocity. Moreover, its absolute flux is less in the smaller-beam cube, indicating that the beam is not recovering all of the flux and thus implying that the feature is (partially) spatially resolved. Considering the arguments presented in Section 3.6, we conclude that this feature represents real emission from compact, high-velocity molecular gas near the nucleus.

Since we argue that this molecular gas is a nuclear outflow (Section 4.3), the fact that it is partially spatially resolved by the smaller-beam observations allows us to constrain the outflow radius to be in the range $88 < \Delta R < 182$ pc ($0.042 < \Delta R < 0.083$ arcsec; i.e. half of the beam major axes of the two observations). Considering that the feature does not appear to be spatially resolved in the channel maps (Section 3.5; Fig. 5) produced from the combined datacube (beam size: 0.113×0.091 arcsec; see Section 2), this indicates that it is partially spatially-resolved in our observations – we thus take 120 pc (0.0545 arcsec) as an upper limit on the outflow radius.

This paper has been typeset from a $\text{\TeX}/\text{\LaTeX}$ file prepared by the author.